Matter

Article

Contextualized synthesis of phenanthroline-based isomeric linkers at heterointerfaces enables stable inverted perovskite solar cells

Graphical abstract

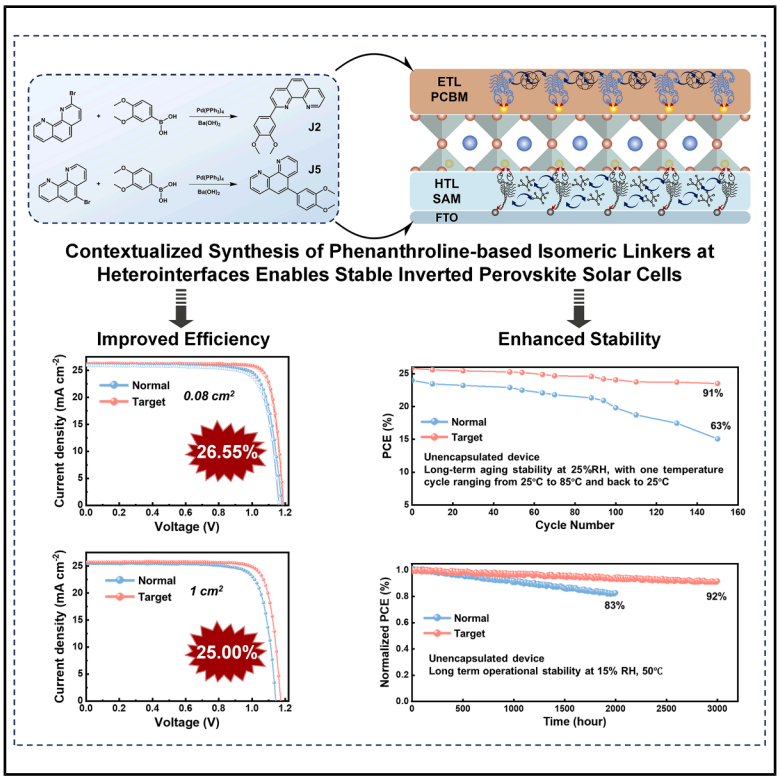

Highlights

- Two phenanthroline-based isomers (named J2 and J5) were rationally synthesized
- J2 and J5 adaptively anchor to charge transport layers, enhancing interface stability
- Efficiencies of 26.55% and 25.00% are achieved for 0.08 cm^2-PSC and 1 cm^2-PSC

Authors

Shujie Qu, Changxu Sun, Fu Yang, ..., Zhiwei Wang, Peng Cui, Meicheng Li

Correspondence

hhuang@ncepu.edu.cn (H.H.), mcli@ncepu.edu.cn (M.L.)

In brief

This work tackles the heterointerface stability in perovskite solar cells by contextually synthesizing phenanthroline-based isomers to reduce interface defects and enhance interfacial adhesion. The resulting devices achieve a champion efficiency of 26.55% and retain 92% of their efficiency after operating for 3,000 h under 1-sun illumination.

6 Development
Practical, real world, technological considerations and constraints

Qu et al., 2026, Matter 9, 102525
February 4, 2026
https://doi.org/10.1016/j.matt.2025.102525

CellPress

Please cite this article in press as: Qu et al., Contextualized synthesis of phenanthroline-based isomeric linkers at heterointerfaces enables stable inverted perovskite solar cells, Matter (2025), https://doi.org/10.1016/j.matt.2025.102525

Matter

CellPress

Article

Contextualized synthesis of phenanthroline-based isomeric linkers at heterointerfaces enables stable inverted perovskite solar cells

Shujie Qu,[1] Changxu Sun,[1] Fu Yang,[1] Hao Huang,[1,*] Shuxian Du,[1] Tongtong Jiang,[1] Qiang Zhang,[1] Luyao Yan,[1] Zhineng Lan,[1] Yingying Yang,[1] Zhiwei Wang,[1] Peng Cui,[1] and Meicheng Li[1,2,*]

[1]State Key Laboratory of Alternate Electrical Power System with Renewable Energy Sources, North China Electric Power University, Beijing 102206, China

[2]Lead contact

*Correspondence: hhuang@ncepu.edu.cn (H.H.), mcli@ncepu.edu.cn (M.L.)

https://doi.org/10.1016/j.matt.2025.102525

PROGRESS AND POTENTIAL In recent years, inverted perovskite solar cells (PSCs) have emerged as a promising photovoltaic technology, garnering significant attention. Their certified efficiency in single-junction configurations has now surpassed 27.0%. However, stability, an issue closely related to the heterointerface, has always been a key factor limiting the future commercialization of inverted PSCs. In this work, two novel phenanthroline-based isomers (named J2 and J5) were rationally designed and synthesized to address the heterointerface stability in inverted PSCs. The reaction sites at positions 2 and 5 were precisely engineered through Suzuki-Miyaura coupling, leading to the successful synthesis of J2 and J5. These molecules seamlessly adapt to both the top and bottom interfaces, with J2 exhibiting co-directional binding ability and J5 demonstrating opposite-directional binding ability. As a result, the inverted 0.08 cm^2-PSCs and 1 cm^2-PSCs achieved power conversion efficiencies (PCEs) of 26.55% and 25.00%, respectively. The device showed enhanced stability, retaining 92% of its initial PCE after 3,000 h of operation under 1-sun illumination. This work proposes a new concept and strategy for enhancing heterointerface stability by contextually designing and synthesizing novel functional materials based on practical heterointerface properties, which is of great significance for promoting the commercialization of inverted PSCs.

SUMMARY

The commercialization of inverted perovskite solar cells (PSCs) is urgently limited by stability, an issue closely related to the heterointerface. In this work, we rationally synthesized two phenanthroline-based isomers—2-(3,4-dimethoxyphenyl)-1,10-phenanthroline (J2) and 5-(3,4-dimethoxyphenyl)-1,10-phenanthroline (J5)—as novel interfacial modifiers to enhance the interface stability. The J2 with co-directional binding sites was incorporated into [6,6]-phenyl-C_{61}-butyric acid methyl ester (PCBM) to interact with it in a π-π manner and coordinate with perovskite, strengthening the interface adhesion. The J5 with opposite-directional binding sites was incorporated into MeO-4PACz to π-π interact with it and coordinate with the FTO substrate and perovskite, respectively, thus stabilizing MeO-4PACz and reinforcing interface. Owing to the improved interfacial mechanical durability and reduced interfacial carrier recombination, the 0.08 cm^2-PSC and 1 cm^2-PSC achieved efficiencies of 26.55% and 25.00%, respectively. Moreover, unencapsulated devices can retain 92% of their initial efficiency after operating 3,000 h under continuous 1-sun illumination and 91% after 150 harsh thermal cycles.

INTRODUCTION

Metal-halide perovskite solar cells (PSCs) have reached certified efficiency exceeding 27.0% in single-junction configurations, emerging as a leading technology for the next photovoltaic revolution.[1–5] Specifically, inverted PSCs have attracted extensive interest owing to their simplified fabrication, efficient carrier extraction, and compatibility with tandem solar cells. In the past few years, inverted PSCs have achieved significant breakthroughs in terms of efficiency.[6–8] However, the stability issue is still the key bottleneck limiting the devices' practical applications. In a multi-layered device, the degradation of heterointerfaces

Please cite this article in press as: Qu et al., Contextualized synthesis of phenanthroline-based isomeric linkers at heterointerfaces enables stable inverted perovskite solar cells, Matter (2025), https://doi.org/10.1016/j.matt.2025.102525

between perovskite and charge transport layers (CTLs) has been reported to be the main reason for the PSCs' performance decay under operation conditions. Considering the massive defect, complex bonding, and relatively higher chemical reaction at the heterointerfaces, understanding the interface degradation mechanism and enhancing the interface stability compatible with the efficiency improvement are necessary for achieving efficient and stable inverted PSCs.[9–11]

The inverted PSCs are inevitably subjected to the external factors of heat, illumination, electric fields, and their complex function in the practical applications. Comparing the functional layers of the perovskite absorber and CTLs, the heterointerfaces between perovskite and CTLs are more easily impacted due to the complex bonding from the different materials and potential chemical reactions. The harmful broken bonding and chemical reactions at the heterointerfaces result in the non-radiative carrier recombination, the initial localized dissociation, and material degradation sites, affecting both the device efficiency and long-term chemical stability. For instance, Chen et al. highlighted that the bond dissociation and chemical reactions at these interfaces contribute to the formation of trap states, which increase the rate of non-radiative recombination, thereby reducing efficiency.[12] Furthermore, Tang et al. also identified that defective interfaces are crucial in triggering recombination losses and hindering effective charge extraction, especially due to weak interface bonding, which compromises the mechanical and chemical stability of the devices.[13]

To enhance the interface stability, various interfacial engineering strategies have been proposed, including buffer layers, interfacial defect passivation, bonding enhancement, and so on.[14,15] Among them, enhancing the bonding between the perovskite and CTL to construct an ordered and robust interface is an effective approach to impede the interface dissociation and degradation. For example, Cai et al. designed bifunctional molecular linkers that markedly strengthened interfacial adhesion while effectively suppressing ion migration and interfacial degradation by forming robust chemical bonds at the perovskite/CTL interface.[16] Besides directly regulating the interfacing bonding between perovskite absorber and CTL, introducing the functional molecular modifiers to serve as linkers is also feasible to enhance the interface robustness. Zhang et al. proposed a multifunctional interfacial molecular bridging strategy that realizes synergistic chemical coordination and π-π stacking at the top interface, enhancing interface adhesion and defect passivation.[17] Due to the rigid planar framework with three fused benzene rings, two vicinal nitrogen atoms with coordination ability, and modifiable sites for tailored functionalization with substituents, the phenanthroline is commonly used as building blocks for functional materials in perovskite devices. This versatile coordination properties make it ideal for enhancing defect passivation and improving charge transport, thereby boosting the efficiency and stability of PSCs.[18,19] For example, Fei et al. introduced phenanthroline-based chelating molecules into the hole transport layer, which selectively coordinate with Pb^{2+} ions in the perovskite, effectively passivating interface defects and the amorphous regions of the film.[20] In addition, Gong et al. utilized a phenanthroline-based silver-coordination-induced n-doping strategy in [6,6]-phenyl-C_{61}-butyric acid methyl ester (PCBM), where the DCBP molecule chelates with silver, releasing free electrons into PCBM, enhancing electron extraction, and boosting the efficiency and stability of inverted PSCs.[21] Although the introduction of functional molecules can effectively enhance interfacial bonding, designing molecular structure and interfacial bonding based on the fundamental properties of interfaces remains a key challenge. Moreover, most studies have focused on optimizing a specific interface or a single CTL, and achieving simultaneous regulation of both interfaces using custom functional materials still presents substantial challenges. Therefore, it is highly desired to precisely design functional materials according to the practical interface property to concurrently stabilize both top and bottom heterointerfaces, further enhancing the interface and device stability.

In this work, we proposed a rational customized molecular-engineering strategy based on a phenanthroline core structure for enhancing the stability of both top and bottom heterointerfaces. Specifically, we designed and synthesized two novel phenanthroline-based isomers—2-(3,4-dimethoxyphenyl)-1,10-phenanthroline (J2) and 5-(3,4-dimethoxyphenyl)-1,10-phenanthroline (J5)—by precisely tuning the reactive sites at positions 2 and 5 via the Suzuki-Miyaura coupling reaction. Benefiting from their π-conjugated systems and selective metal coordination, the J2 and J5 molecules can serve as the cross-linker at both heterointerfaces through simultaneously interacting with the perovskite and CTLs, which enhances the interfacial mechanical durability and reduces the interfacial non-radiative carrier recombination. These advantages contribute to highly efficient and highly stable inverted PSCs, achieving a champion efficiency of 26.55% for a device with an aperture area of 0.08 cm^2 and 25.00% for a device with an aperture area of 1 cm^2. Encouragingly, the unencapsulated devices can retain 94% of their initial efficiency after 4,000 h of storage under ambient air conditions, maintain 92% of their initial efficiency after 3,000 h of continuous operation under 1-sun illumination, and sustain 91% of their initial efficiency after undergoing rigorous thermal cycling.

RESULTS AND DISCUSSION

Molecular design and synthesis

Previous studies have highlighted that addressing interface stability issues is crucial for the photovoltaic performance and long-term stability of inverted PSCs. As illustrated in Figure 1A, during the operated condition or harsh aging condition of high temperature, bias voltage, or UV illumination, the heterointerface undergoes defect formation, mechanical dissociation, and materials degradation, which further induce the photovoltaic performance decay and device failure.[22,23] To enhance the device stability, contextually designing and synthesizing the functional molecules to construct additional bonding in a bridged manner based on the practical interfacial properties is an effective strategy. In inverted PSCs, considering the commonly used π-conjugated CTLs of [4-(3,6-dimethoxy-9H-carbazol-9-yl)butyl]phosphonic acid (MeO-4PACz) and [6,6]-phenyl C_{61} butyric acid methyl ester (PCBM), we selected phenanthroline as the core scaffold due to its inherent π-conjugation property (Figure 1B).[24] Specifically, 2-bromo-1,10-phenanthroline and 5-bromo-1,10-phenanthroline were selected as the reaction

Please cite this article in press as: Qu et al., Contextualized synthesis of phenanthroline-based isomeric linkers at heterointerfaces enables stable inverted perovskite solar cells, Matter (2025), https://doi.org/10.1016/j.matt.2025.102525

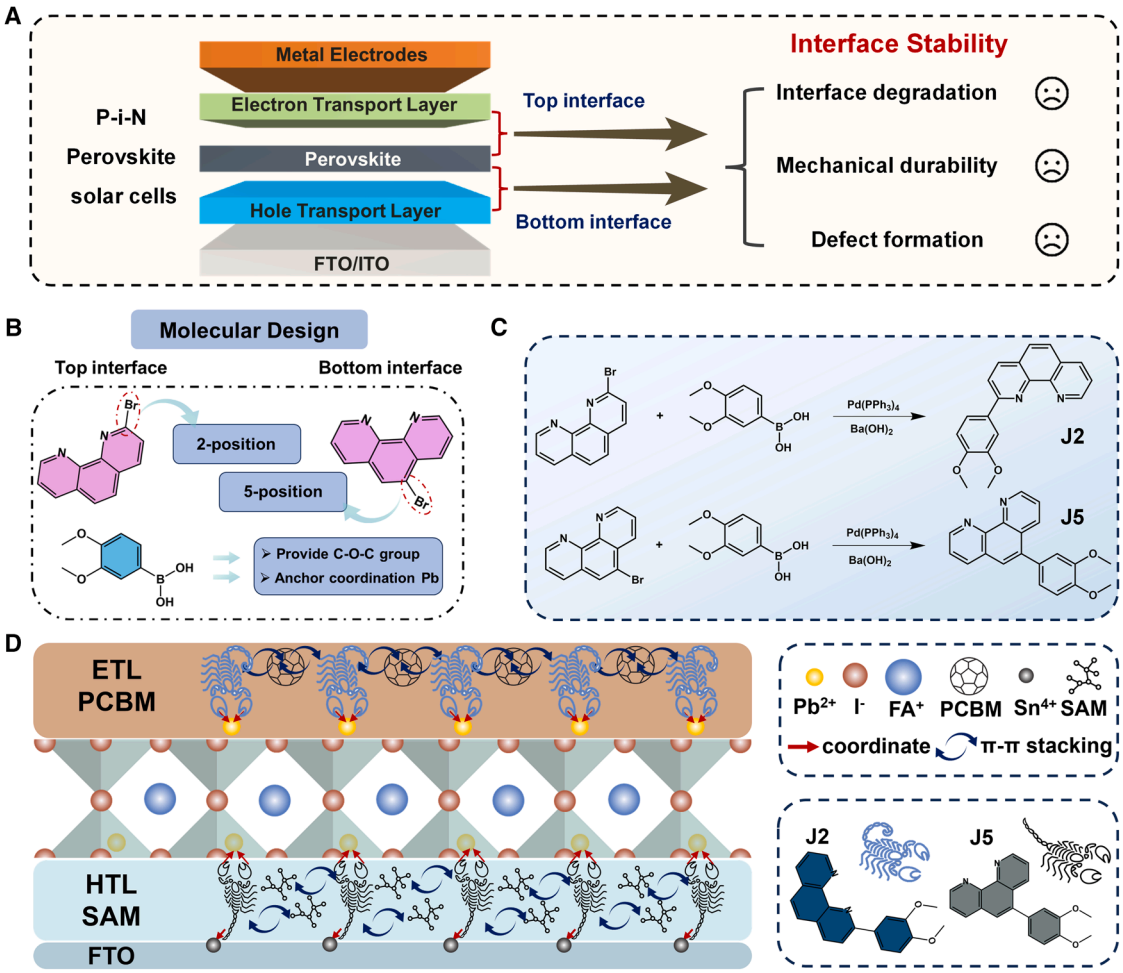

Figure 1. Molecular design and synthesis

(A) Interface stability issues in inverted PSCs.

(B) Design strategy for customized phenanthroline-based isomers.

(C) Synthetic routes for J2 and J5 molecules via Suzuki-Miyaura reaction.

(D) Schematic illustration of interface stabilization.

materials, in which the Br site is utilized to decide the substitution site, allowing the subsequent synthesis of site-selective derivatization. Meanwhile, to enable effective bonding with perovskite film, 3,4-dimethoxyphenylboronic acid (Figure 1B) was chosen as a substituent to replace the bromo group of phenanthroline-based materials, leading to the customized phenanthroline-based isomers. As shown in Figure 1C, the Suzuki-Miyaura cross-coupling reaction was employed as the key synthetic strategy to successfully obtain J2 and J5, which were validated by nuclear magnetic resonance spectroscopy (NMR; Figures S1 and S2).[25] Their NMR spectra were well resolved, with all protons accounted for, confirming both the success of the coupling and the integrity of their respective substituents. In detail, the J2 molecule possesses a molecular geometry favorable for π-π stacking interactions with the electron transport layer of PCBM, while its terminal methoxy groups enable bridge-connecting with the perovskite film. This feature of the co-directional binding site makes the J2 molecule a modifier at the PCBM/interface. The J5 molecule is designed to serve as a modifier at MeO-4PACz/perovskite, considering its feature as an opposite-directional binding site. The J5 has the potential to simultaneously form the π-π stacking interactions with the hole transport layer of MeO-4PACz and the coordination bonding with perovskite but can also form a coordination bonding with FTO substrate through N atom in phenanthroline group. The additional bonding with substrate is supposed to further stabilize the MeO-4PACz molecule and reinforce the interfacial interaction, thereby enhancing the stability of MeO-4PACz/perovskite interface.[26] A schematic illustration of the abovementioned interface stabilization through two customized novel phenanthroline-based isomers is shown in Figure 1D.

Strengthened interface adhesion

We designed the J2 molecule to reinforce the perovskite/PCBM interface and the J5 molecule to reinforce the MeO-4PACZ/perovskite interface, considering their molecular features. In

Please cite this article in press as: Qu et al., Contextualized synthesis of phenanthroline-based isomeric linkers at heterointerfaces enables stable inverted perovskite solar cells, Matter (2025), https://doi.org/10.1016/j.matt.2025.102525

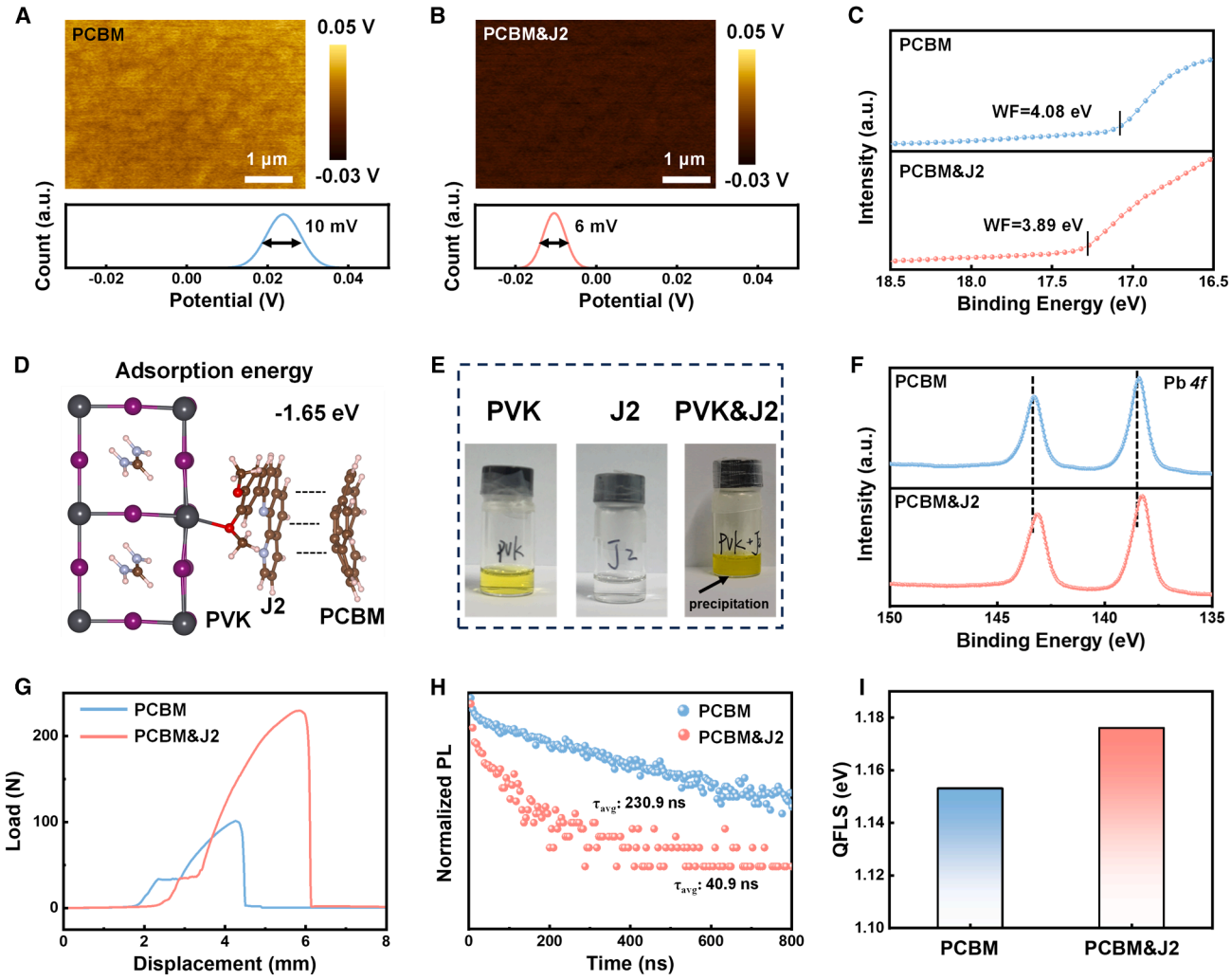

Figure 2. Top interface stability

(A and B) KPFM images of the PCBM and PCBM&J2 films.
(C) UPS spectra of the perovskite/PCBM and perovskite/PCBM&J2 films.
(D) DFT calculation of the interaction of J2 with perovskite and PCBM.
(E) Photo of the different solutions.
(F) XPS spectra of Pb 4f from the perovskite/PCBM and perovskite/PCBM&J2 films.
(G) The load-distance curves of the ITO-PEN/PCBM/perovskite films.
(H) TRPL spectra of the perovskite/PCBM and perovskite/PCBM&J2 films.
(I) QFLS data of the devices with an FTO/perovskite/PCBM structure.

our experiments, the device architecture is FTO/MeO-4PACz/Perovskite/PCBM/2,9-dimethyl-4,7-diphenyl-1,10-phenanthrolin (BCP)/Ag. J2 was added to PCBM solution with a concentration of 5 mM, while J5 was added to MeO-4PACz solution with a concentration of 1 mM. Here, we first explore the role of the J2 molecule on the perovskite/PCBM interface. Considering that the J2 molecule was incorporated into the PCBM, we explored the influence of J2 on the PCBM film before researching the interfacial property. The Kelvin probe force microscopy (KPFM) measurement was used to characterize the PCBM with and without the J2 molecule.[27] As shown in Figures 2A and 2B, the PCBM&J2 exhibits a lower surface potential with a more uniform distribution, indicating that J2 molecules may lead to a more ordered molecular arrangement of PCBM. The decreased surface potential after incorporating J2 indicates an upshift of the Fermi level, which is validated by ultraviolet photoelectron spectroscopy (UPS) measurements, showing a decrease in the work function from 4.08 eV to 3.89 eV (Figure 2C). The incorporation of the J2 molecule into PCBM was designed to enhance the interaction between PCBM and perovskite, considering its molecular feature mentioned before. We investigated the interactions of the J2 molecule at the perovskite/PCBM interface. As shown in Figure S3, density functional theory (DFT) calculations indicate that the adsorption energies of J2 with PCBM and

Please cite this article in press as: Qu et al., Contextualized synthesis of phenanthroline-based isomeric linkers at heterointerfaces enables stable inverted perovskite solar cells, Matter (2025), https://doi.org/10.1016/j.matt.2025.102525

perovskite are −0.34 eV and −1.05 eV, respectively, suggesting that J2 can bind significantly to each component individually. Furthermore, the adsorption energy of J2 with both PCBM and perovskite is −1.65 eV (Figures 2D andS4), indicating a feasible bridge-linking at the interface. Specifically, the phenanthroline moiety of J2 forms π-π stacking interactions with PCBM, while the methoxy group binds to the perovskite surface through a Pb-O interaction. To visualize the interaction between J2 and perovskite, we directly added the J2 into the perovskite precursor, and a faint yellow precipitate can be observed even at a low concentration of J2 (<0.1 mg mL^{-1}; Figure 2E).[17] This formed precipitate is primarily attributed to the coordination between Pb^{2+} and J2. To validate this coordination, we directly characterized the perovskite/PCBM film using X-ray photoelectron spectroscopy (XPS). As shown in Figure 2F, the downshift of the Pb 4f core levels after incorporating the J2 molecule demonstrates the interaction between perovskite and J2. Considering the N atom in the phenanthroline, which can also interact with Pb^{2+} in perovskite, we conducted an additional experiment to explore the preferability of the interaction of Pb–O or Pb–N.[28] We added PbI_2 to a J2 solution (solvent was DMF) and then deposited the mixed film. The XPS characterization was performed on this film, with the results showing that the N 1s peaks at 401.30 eV (C–N) and 398.74 eV (C=N) showed no shift upon the addition of PbI_2, and the C–O peak shifts from 533.41 eV to 533.70 eV, indicating that the O in methoxy group coordinates with Pb^{2+} rather the N in phenanthroline (Figure S5). This preferred interaction of Pb–O is also consistent with the DFT results. To explore the influence of J2 on the interface mechanical adhesion, an experiment to evaluate the adhesion strength was designed. Specifically, the FTO substrate was replaced with a flexible ITO-PEN substrate to eliminate the influence of substrate rigidity on the test results. The PCBM layer was first deposited on the ITO-PEN, followed by the deposition of the perovskite film. Subsequently, a clean ITO-PET substrate was attached to the top surface of the ITO-PEN/PCBM/perovskite structure using a UV-curable adhesive. The assembly was then subjected to a tensile test using a universal mechanical testing machine to peel off the perovskite film from the ITO-PEN/PCBM structure (the mechanism is illustrated in Figure S6),[16] thereby quantitatively evaluating the adhesion strength between the PCBM and perovskite. As shown by the load-distance curves (Figure 2G), the target film exhibited a maximum tensile force of 230.7 N, which is significantly higher than the 100.3 N observed for the normal film. This result demonstrates the enhanced interface adhesion strength between the PCBM and perovskite film due to the incorporation of J2, which contributes to improving interface mechanical durability. The constructed interfacial cross-linking and optimized PCBM electron transport layer should contribute to the promoted interfacial electron extraction and reduced interfacial non-radiative carrier recombination, which were subsequently explored using measurements of time-resolved photoluminescence (TRPL) and quasi-Fermi level splitting (QFLS) analysis.[29–34] As shown in Figure 2H and Table S1, the TRPL data reveal that τ_1 decreases from 7.79 to 4.14 ns, and the average carrier lifetime (τ_{avg}) decreases from 230.9 to 40.9 ns after incorporating the J2 into PCBM, indicating the promoted interfacial carrier extraction.[29,35,36] Furthermore, devices structured as FTO/perovskite/PCBM (PCBM&J2) were fabricated for QFLS analysis. The results reveal that the sample with PCBM&J2 shows a higher QFLS, which may result from the reduced interfacial non-radiative recombination (Figure 2I) and the decreased work function of PCBM. Based on the above results and discussion, the J2 molecule can construct a cross-linking at the perovskite/PCBM interface through interacting with PCBM in a manner of π-π stacking and interacting with perovskite via Pb–O bonds, which effectively reduces the interfacial carrier non-radiative recombination and reinforces the interfacial mechanical stability.

After discussing the role of J2 at the perovskite/PCBM interface, we now turn our attention to the role of J5 at the MeO-4PACz/perovskite interface, which is the buried interface in the inverted PSCs. We incorporated J5 into MeO-4PACz solution and revealed that the J5 molecule can homogenize the MeO-4PACz dispersion, which can be demonstrated by the KPFM results (Figures 3A and 3B). The modification of MeO-4PACz dispersion may be due to J5 forming stable π-π stacking interactions with MeO-4PACz (Figure S7), which weakens lateral SAM-SAM interactions and suppresses aggregation, thereby promoting a more ordered and uniform monolayer. This optimized MeO-4PACz dispersion can also be validated by the XPS results (as shown in Figure S8; Table S2; and Note S1). The optimized MeO-4PACz dispersion also influences its energy level structure. The average surface potential of MeO-4PACz increases from 0.126 to 0.138 V after incorporating J5 molecules, which is consistent with the UPS result that the work function increased from 5.02 to 5.14 eV (Figure S9). This result indicates that the incorporation of J5 contributes to a more uniform MeO-4PACz layer with increased work function, which is beneficial for the interfacial hole extraction. A smooth and ordered SAM dispersion is expected to be favorable for perovskite film deposition. After J5 modification, the X-ray diffraction (XRD) characterization indicates that the crystallographic orientation of the perovskite (100 and 200 planes) was enhanced, with no other secondary phases detected (Figure S10). This optimized perovskite crystallization can also be supported by the cross-sectional SEM images (Figure S11). Except for the MeO-4PACz optimization, the J5 molecule was designed to reinforce the interface through anchoring the MeO-4PACz and cross-linking the interface. We first performed the DFT calculations to explore the preferred absorption of the J5 molecule on the FTO substrate, considering the MeO-4PACz deposited earlier than the perovskite. As shown in Figures 3C and S12, the J5 molecule possesses metal-coordinating N and O sites, with adsorption energies to SnO_2 of −1.57 and −0.98 eV, respectively, indicating that the J5 preferentially coordinates with Sn^{4+} ions through N in phenanthroline. Based on this model, we further refined and extended the DFT calculations on the interaction manner of J5 at the interface. Since the π-π stacking effect between MeO-4PACz and J5 is relatively weaker than the coordination interaction, we therefore focused on investigating the coordination interactions of J5 with both FTO and perovskite. As shown in Figure 3D, the adsorption energy of J5 with SnO_2 and perovskite is −2.03 eV, which confirms the feasibility of the interfacial bridge-linking. In addition, to verify the interaction between J5 and perovskite, a visualized experiment was carried out. As

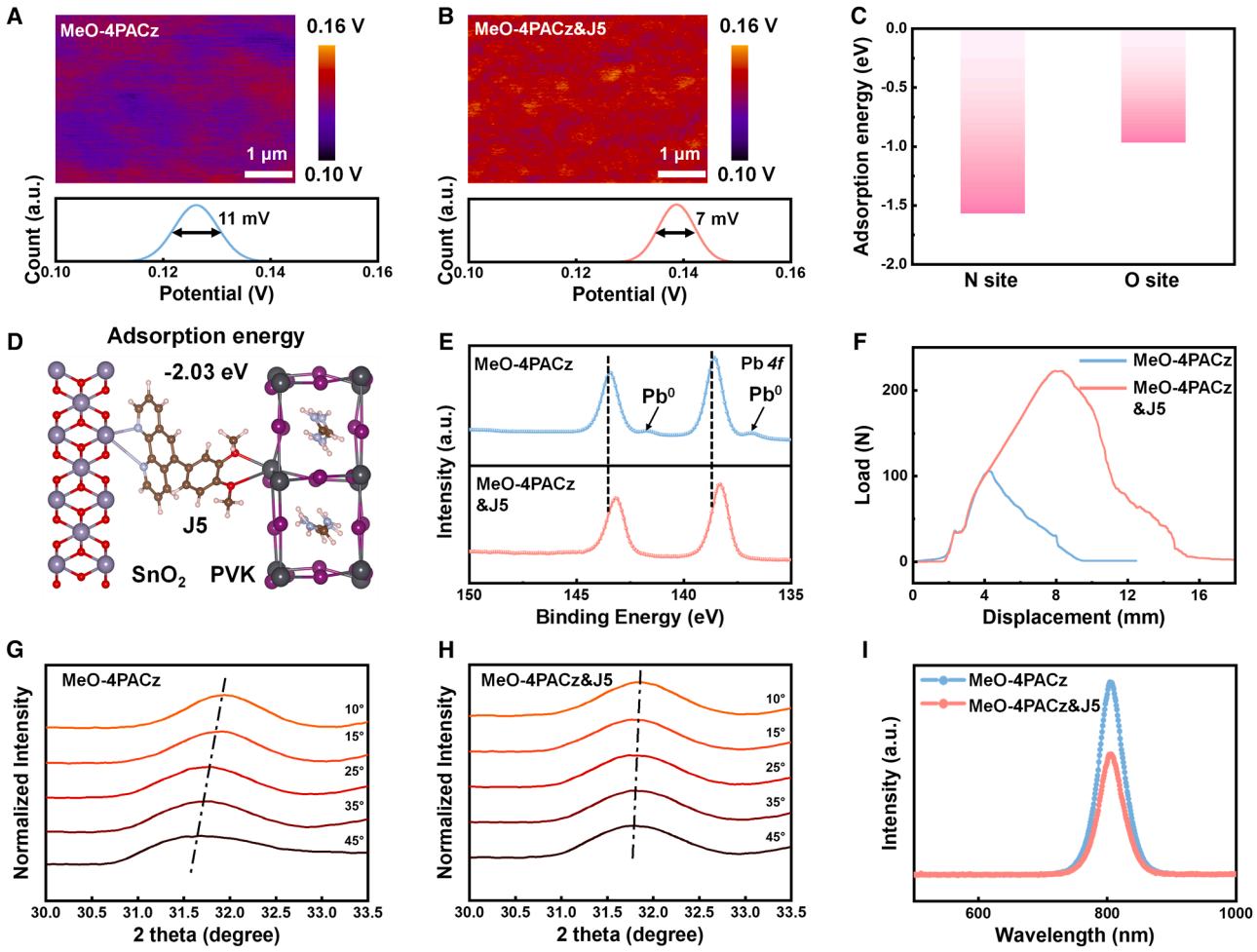

Figure 3. Bottom interface stability

(A and B) KPFM images of the MeO-4PACz/perovskite and MeO-4PACz&J5/perovskite films.

(C) DFT calculation results of the interaction between J5 and SnO_2 (N site and O site).

(D) DFT calculation of the interaction of J5 with SnO_2 and perovskite.

(E) XPS spectra of Pb 4f from the buried MeO-4PACz/perovskite and MeO-4PACz&J5/perovskite films.

(F) The load-distance curves of the ITO-PEN/MeO-4PACz/perovskite films.

(G and H) GIXRD patterns at different tilt angles of the MeO-4PACz/perovskite and MeO-4PACz&J5/perovskite films at incident angle 0.3° (from top to bottom: φ = 10°, 15°, 25°, 35°, and 45°).

(I) PL spectra of the MeO-4PACz/perovskite and MeO-4PACz&J5/perovskite films.

shown in Figure S13, when J5 was mixed with the perovskite precursor solution, a faint yellow precipitate formed even at very low J5 concentrations (below 0.1 mg/mL), which demonstrates the coordination behavior between J5 and perovskite. Similarly, using our previously reported method,[37] we peeled off the perovskite to expose the buried surface and then performed XPS analysis. An evident downshift of the Pb 4f core levels was observed, and no Pb^0 species were detected in the target film (Figure 3E). The peak shift of Pb 4f should result from the interaction between J5 and perovskite through the O–Pb bond, and suppressed Pb^0 defects may stem from the passivated undercoordinated Pb^{2+} by J5.

The influence of J5 on the interface mechanics adhesion was researched by testing the load-distance curves as described above (the mechanism is illustrated in Figure S14). When the substrate changed from FTO to ITO-PEN, the J5 was demonstrated to show a similar effect on the SAM deposition (Figure S15). The device structured as ITO-PEN/MeO-4PACz (MeO-4PACz&J5)/perovskite was tested. The results show that the device with J5 possesses a tensile force of 218.9 N, approximately twice that of device without J5. Based on this interface bridge-linking, we further characterize the perovskite residual stress, an issue closely related to the interface property. The grazing-incidence X-ray diffraction (GIXRD) combined with the 2θ-$\sin^2\varphi$ method was employed to quantify the residual stress at a depth of approximately 200 nm from the perovskite film surface (Figures 3G and 3H).[38–40] The negative slope obtained from the linear fitting of the 2θ-$\sin^2\varphi$ method indicates the presence of residual tensile stress in

Please cite this article in press as: Qu et al., Contextualized synthesis of phenanthroline-based isomeric linkers at heterointerfaces enables stable inverted perovskite solar cells, Matter (2025), https://doi.org/10.1016/j.matt.2025.102525

perovskite films on both types of MeO-4PACz (Figure S16). Notably, the perovskite film on MeO-4PACz&J5 exhibits lower tensile stress compared to the perovskite film on MeO-4PACz. This can be attributed to the more compact and ordered MeO-4PACz layer, which reduces local shrinkage gradients and film thickness fluctuations of perovskite film during annealing and cooling processes. The reduced tensile stress of perovskite film can further contribute to forming a robust interface, collaboratively assisting in improving interfacial mechanical durability. The optimized MeO-4PACz dispersion and interface bridge-linking are supposed to promote the interface carrier transport and reduce the interface carrier non-radiative recombination, which are explored by various measurements regarding the film carrier dynamics. First, photoluminescence (PL) and TRPL measurements were performed on the MeO-4PACz/perovskite samples, demonstrating that the perovskite film on MeO-4PACz&J5 exhibits lower PL intensity (Figure 3I) and a smaller average carrier lifetime (τ_{avg}) (Figure S17), indicating the promoted interfacial carrier transport. In addition, QFLS analysis was carried out for the devices of FTO/MeO-4PACz (MeO-4PACz&J5)/perovskite, with the results showing that the device with J5 consistently shows a lower QFLS loss (Figure S18). In short, the J5 can optimize the MeO-4PACz dispersion and strengthen interface adhesion, which contributes to the reduced interface carrier non-radiative recombination and enhanced interface mechanical stability.

Photovoltaic performance of PSCs

We have experimentally demonstrated that J2 and J5 can promote the interfacial carrier transport and enhance interface mechanical stability for the heterointerfaces of perovskite/PCBM and MeO-4PACz/perovskite, respectively. We further explore the influence of J2 and J5 on the photovoltaic performance of the inverted PSCs. For clarification, the sample with J2 in PCBM and J5 in MeO-4PACz is named as target, and the sample without J2 and J5 is named as normal. To explore the impact of J2 and J5 on the power conversion efficiency (PCE) of PSCs, 25 independently fabricated devices were prepared for both the normal and target PSCs. As shown in Figure 4A, both types of devices exhibit good reproducibility, and the Target devices exhibit higher average PCE values. Encouragingly, the champion target PSC (the active area is 0.08 cm^2) achieves a PCE of 26.55% (J_{SC} = 26.21 mA cm^{-2}, V_{OC} = 1.193 V, FF = 84.92%) with negligible hysteresis (Figure 4B; Table S3), demonstrating a significant improvement compared to the normal PSC, which shows a PCE of 24.68% (J_{SC} = 26.03 mA cm^{-2}, V_{OC} = 1.174 V, FF = 80.77%). The target integrated short-circuit current density derived from the external quantum efficiency (EQE) spectrum (Figure 4C) is 25.71 mA cm^{-2}, demonstrating only a minor deviation from the current density obtained from the *J-V* measurements.

We further scaled up the PSCs to an active area of 1 cm^2. As shown in Figure 4D and Table S4, the champion target device achieved a PCE of 25.00% (J_{SC} = 25.71 mA cm^{-2}, V_{OC} = 1.174 V, FF = 82.84%), while the normal device reached only 23.27% (J_{SC} = 25.52 mA cm^{-2}, V_{OC} = 1.147 V, FF = 79.49%). The performance parameters of the other 10 target devices are summarized in Table S5 with an average PCE of 24.27%. These results demonstrated that joint incorporation of J2 and J5 can effectively improve the photovoltaic performance of PSCs, and this strategy shows a universality in fabricating high-efficiency large-area PSCs. In addition, these novel functional materials can also be directly served as interfacial modifiers, showing a positive effect on enhancing the photovoltaic performance of the PSCs (Figure S19). Finally, we also tested the versatility of J2 and J5 by applying J2 to the C_{60} layer and J5 to the Me-4PACz layer. As shown in Figure S20, the target devices showed significant efficiency improvement, demonstrating that our molecular tailoring strategy can be broadly applied to various interfacial materials.

Next, we delve deeper into the reasons behind the enhancement of device performance. Firstly, we conducted dark current measurements on PSCs with the results shown in Figure S21. The target PSCs exhibited a significantly lower dark saturation current density (J_0), indicating the suppressed non-radiative recombination. We examined the correlation between V_{OC} and light intensity based on the relation $V_{OC}=(n_{ID}k_BT/q)*\ln(I)$ (where k_B is the Boltzmann constant, and q is the elementary charge). The extracted ideality factors (n_{ID}) are 1.49 for the target PSCs and 1.82 for the normal PSCs (Figure 4E). A smaller n_{ID} value implies less trap-assisted recombination within the device, which is consistent with the dark current results. The trap-assisted recombination within the device can also be explored by the electrochemical impedance spectroscopy (EIS) characterization and electroluminescence (EL) efficiency (EQE_{EL}). In the EIS spectra (Figure 4F), the target device exhibits a larger recombination resistance than that of normal device, indicating the reduced trap-assisted recombination. As for the EL characterization, the target device exhibits significantly higher EL intensity than the normal device, reflecting reduced non-radiative losses (Figure 4G). Under identical injection current conditions, the EQE_{EL} of the target device shows a marked improvement over that of the normal device, consistent with its higher EL efficiency (Figure S22). The characterization results of Space-charge-limited current (SCLC) and the trap density of states (tDOS) reveal the reduced density of defect states in PSCs, which should contribute to the reduced trap-assisted recombination (Figures S23–S25 and Note S2).[41–44] These results regarding the reduced carrier non-radiative recombination mainly explain the significant increase in V_{OC}. To gain a deeper insight into the interfacial carrier transport and recombination dynamic, the measurements of transient photocurrent (TPC) and transient photovoltage (TPV) were also carried out. The photocurrent decay behavior reveals the carrier extraction and transport process in PSCs. The target PSCs exhibit a TPC decay time of 5.73 μs, shorter than that (8.57 μs) of normal PSCs, demonstrating the more efficient interfacial carrier extraction and transport (Figure 4H). The photovoltage decay behavior mainly corresponds to the carrier recombination process in PSCs. The target PSCs show a longer TPV decay time of 4.47 μs than 3.01 μs, which indicates the reduced interfacial carrier recombination (Figure 4I). The tailored interface optimization through contextually designed phenanthroline-based isomeric linkers is demonstrated to promote the interfacial carrier transport and reduce interfacial carrier non-radiative recombination, synergistically contributing to the enhancement in the photovoltaic performance of PSCs.

Improved stability of PSCs

The introduction of J2 and J5 effectively strengthens the interface adhesion, which is expected to show a positive impact on the

Please cite this article in press as: Qu et al., Contextualized synthesis of phenanthroline-based isomeric linkers at heterointerfaces enables stable inverted perovskite solar cells, Matter (2025), https://doi.org/10.1016/j.matt.2025.102525

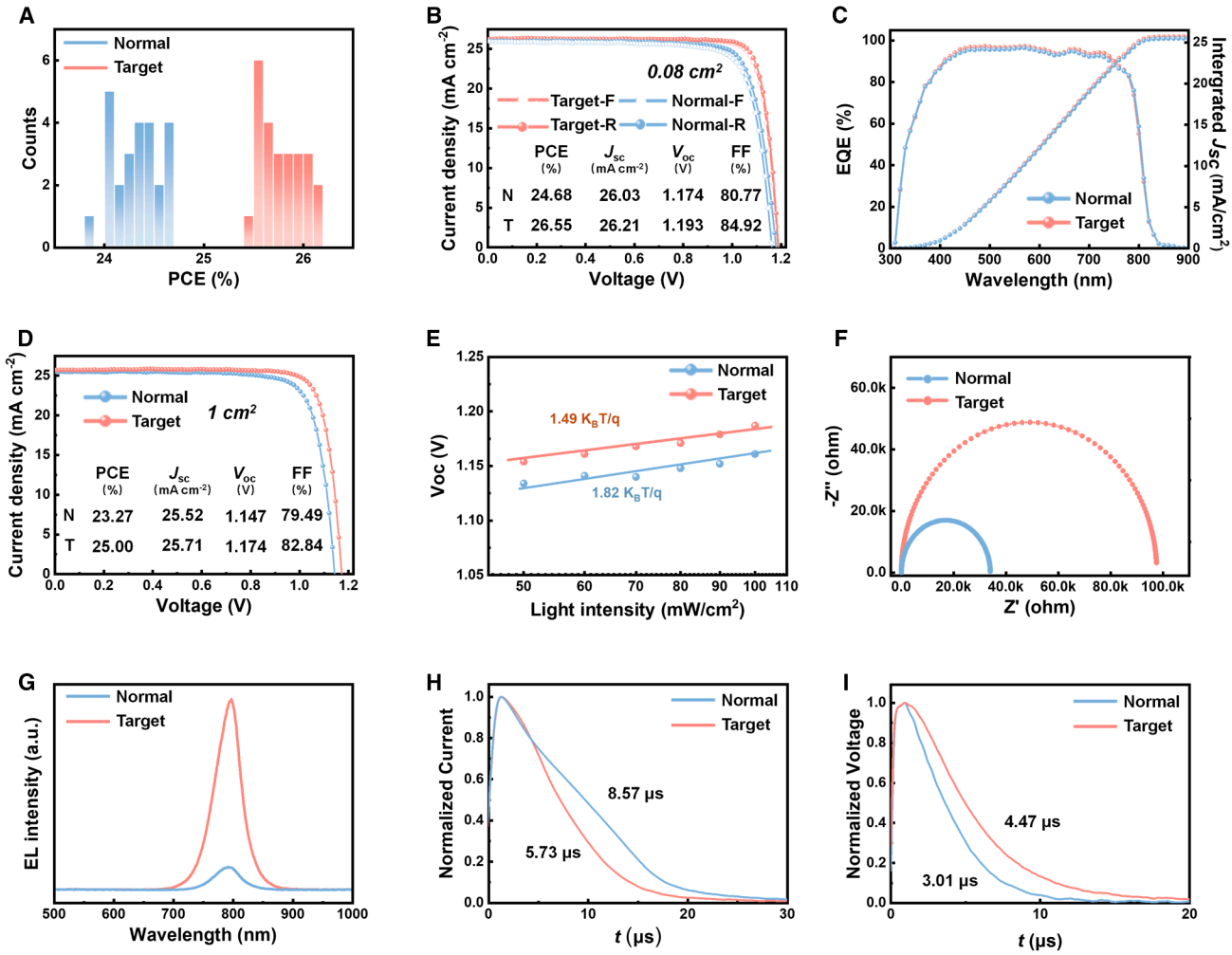

Figure 4. Photovoltaic performance

(A) Distribution of the PCE values of the 25 normal and target PSCs.
(B) *J-V* curves of champion normal and target PSCs with an active area of 0.08 cm^2.
(C) EQE spectra of the normal and target PSCs.
(D) *J-V* curves of champion normal and target PSCs with an active area of 1 cm^2.
(E) V_{OC} of the normal and target PSCs plotted against the logarithm of light intensity.
(F) EIS spectra of normal and target PSCs.
(G) EL spectra of the normal and target PSCs under a 2V bias.
(H) TPC decay curves of the normal and target devices.
(I) TPV decay curves of the normal and target devices.

long-term stability of the inverted PSCs. First, we directly characterize the interface stability. Before stability test, we first demonstrated that the J2/J5 shows negligible influence on the hydrophobicity of PCBM and MeO-4PACz films (Figure S26). The samples were exposed to a humid air environment with a relative humidity (RH) of approximately 45% for 240 h. For the perovskite/PCBM interface, we removed the original PCBM layer by rinsing with chlorobenzene and then characterized the perovskite film by scanning electron microscope (SEM). The chlorobenzene rinsing was demonstrated to show negligible influence on the perovskite surface morphology and structure (Figure S27). As shown in Figure 5A, without the J2 in PCBM, the perovskite film exhibited significant decomposition, whereas the perovskite film under PCBM&J2 showed no obvious signs of decomposition, demonstrating the improved interface stability. As for the buried interface of MeO-4PACz/perovskite, the perovskite film was peeled off and then characterized by SEM. The SEM results also indicate that the incorporation of J5 in MeO-4PACz can enhance the interface stability (Figure 5B). We further used XPS to analyze this buried interface. The unmodified sample showed a clear metallic Pb^0 signal, while the J5-modified sample exhibited significantly suppressed Pb^0 formation (Figure S28). For MeO-4PACz/perovskite/PCBM, XRD was applied. As shown in Figure S29, unmodified films showed δ-phase peaks of perovskite, indicating the perovskite

Please cite this article in press as: Qu et al., Contextualized synthesis of phenanthroline-based isomeric linkers at heterointerfaces enables stable inverted perovskite solar cells, Matter (2025), https://doi.org/10.1016/j.matt.2025.102525

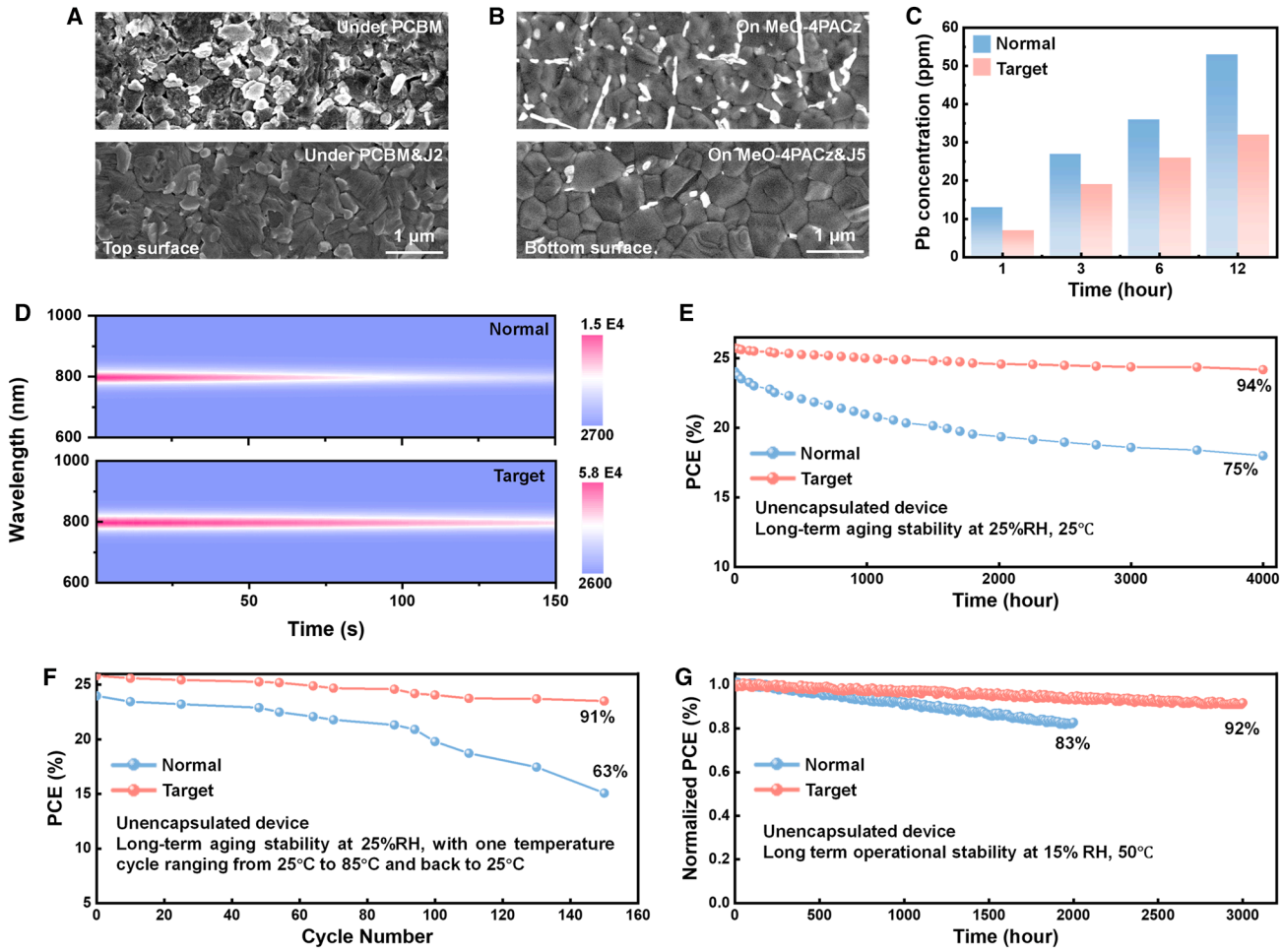

Figure 5. Device stability

(A) SEM images of the perovskite/PCBM and perovskite/PCBM&J2 films. Both films were stored under ambient conditions with an RH of 45% for 240 h, and the PCBM layer was removed by rinsing with chlorobenzene.

(B) SEM images of the buried MeO-4PACz/perovskite and MeO-4PACz&J5/perovskite films. Both films were stored under ambient conditions with an RH of 45% for 240 h.

(C) Lead ion concentration in the soaking solution after immersing the PSCs for various durations.

(D) *In situ* EL mapping of normal and target PSCs; the PSCs were under a bias voltage of 2 V.

(E) Long-term stability of unencapsulated devices stored under ambient conditions of 25% RH and 25°C.

(F) Long-term stability of unencapsulated devices at 25% RH, with temperature cycles ranging from 25°C to 85°C and back to 25°C.

(G) Operational stability of the unencapsulated devices under continuous simulated AM1.5 illumination at the maximum power point and approximately 15% RH, 50°C in a glovebox.

decomposition. In contrast, no δ-phase peaks were observed in films modified with J2 and J5, demonstrating enhanced interface stability and suppressed perovskite degradation. To further verify the interface robustness, we quantified the Pb^{2+} concentration of PSCs in the soaking solution using atomic absorption spectroscopy, as shown in Figure 5C.[45] The analysis reveals a pronounced difference between the two devices, and this difference gradually increases as the soaking time extends from 1 to 12 h. The constructed robust interface is also experimentally demonstrated to contribute to the reduced ion migration in the device (Figure S30; Note S3). This interface stability enhancement should mainly be attributed to the reinforced interface interaction and suppression of interface defects.

We further characterize the device stability. First, we monitored the *in situ* EL of the PSCs to evaluate their operational stability. As shown in Figure 5D, both types of PSCs exhibited high initial EL peak intensities, indicating excellent optoelectronic performance, consistent with the *J-V* results. However, over time, the EL intensity of the normal PSC decreased rapidly. In contrast, the target PSC showed only a slight decrease in EL intensity and maintained significantly greater stability throughout the measurement period. Secondly, we systematically monitored the performance evolution of the unencapsulated PSCs under various conditions. Under ambient conditions (25% RH, 25°C), the target device retained 94% of its initial PCE after 4,000 h of aging, whereas the normal

Please cite this article in press as: Qu et al., Contextualized synthesis of phenanthroline-based isomeric linkers at heterointerfaces enables stable inverted perovskite solar cells, Matter (2025), https://doi.org/10.1016/j.matt.2025.102525

device maintained only 75% (Figure 5E). We conducted an additional critical moisture stability test by placing unencapsulated devices on a condition of 25°C and 45% RH. The results indicate that the target device also shows an enhanced stability (Figure S31). In addition, under more stringent thermal cycling conditions (25°C–85°C–25°C, 35 min per cycle), the target device retained 91% of its initial PCE after 150 cycles, while the normal device retained only 63% (Figure 5F). Furthermore, long-term operational stability, a key indicator for evaluating the reliability of PSCs, was assessed by testing the unencapsulated devices under continuous 1 sun illumination in a glovebox maintained at 15% RH and 50°C. The results show that the target device maintained 92% of its initial PCE after 3,000 h of continuous operation, whereas the normal PSC exhibited significant performance degradation after 2,000 h (Figure 5G). These results clearly demonstrate that the fabricated devices exhibit excellent stability in terms of environmental durability, thermal cycling resistance, and long-term operational reliability. Based on the above stability analyses, it is evident that enhanced interface stability through strengthening the interface adhesion plays a critical role in ensuring the long-term stability of PSCs.

Conclusion

In summary, we have rationally designed and synthesized two novel phenanthroline-based isomers to specifically address the heterointerfaces stability in inverted PSCs. We synthesized the J2 and J5 molecules, which adapted seamlessly to both the top and bottom interfaces by precisely engineering the 2- and 5-position reactive sites through the Suzuki-Miyaura coupling. The J2 and J5 significantly strengthen heterointerface adhesion, benefiting from the π-π stacking and selective metal coordination, thus enhancing interfacial mechanical durability and facilitating carrier transport. Owing to this customized strategy, the optimized inverted PSCs achieve a champion efficiency of 26.55% with an aperture area of 0.08 cm^2 and sustain a high efficiency of 25.00% while enlarging aperture area to 1 cm^2. Furthermore, the device can retain 92% of its initial efficiency after 3,000 h of continuous operation under 1-sun illumination and maintain 91% of its initial efficiency after exposure to rigorous thermal cycling, demonstrating excellent long-term stability. Our work offers fresh mechanistic insight and a practical molecular strategy for overcoming the stability bottleneck regarding the heterointerfaces, thereby providing a new approach to achieve highly efficient and stable PSCs.

METHODS

Materials

All the materials employed in this study were used as received without any further purification. The main chemicals and substrates include FTO glass substrates (Suzhou ShangYang), MeO-4PACz (TCI, >99.0%), PbI_2 (TCI, 99.999%), $PbCl_2$ (Alfa, 99.999%), solvents such as DMF and DMSO (Sigma-Aldrich, 99.9%), chlorobenzene (Sigma-Aldrich, 99.5%), isopropanol (Acros, 99.9%), as well as FAI, MAI, MACl, CsI, PEAI, PCBM, and BCP (all from Xi'an Polymer Light Technology Corp).

Synthesis of J2 and J5 molecules

A mixture of 2-bromo-1,10-phenanthroline (129.5 mg, 0.5 mmol), 3,4-dimethoxyphenylboronic acid (103.9 mg, 0.57 mmol), $Pd(PPh_3)_4$ (57.7 mg, 0.05 mmol), and $Ba(OH)_2$ (315.0 mg, 1 mmol) was dissolved in 10 mL of DME solution. The reaction was carried out under a nitrogen atmosphere, heating to 90°C and stirring overnight. Afterward, the mixture was cooled to ambient temperature. The organic components were extracted using dichloromethane and washed multiple times with brine. The solvent was dried over anhydrous magnesium sulfate, and the solution was filtered. The solvent was evaporated under reduced pressure, and the product was purified by column chromatography (using a mixture of methanol and dichloromethane, 1:20) to yield 2-(3,4-dimethoxyphenyl)-1,10-phenanthroline as a light-yellow solid.

A mixture of 5-bromo-1,10-phenanthroline (129.5 mg, 0.5 mmol), 3,4-dimethoxyphenylboronic acid (103.9 mg, 0.57 mmol), $Pd(PPh_3)_4$ (57.7 mg, 0.05 mmol), and $Ba(OH)_2$ (315.0 mg, 1 mmol) was dissolved in 10 mL of DME solution. The reaction was carried out under a nitrogen atmosphere, heating to 90°C and stirring overnight. Afterward, the mixture was cooled to ambient temperature. The organic components were extracted using dichloromethane and washed multiple times with brine. The solvent was dried over anhydrous magnesium sulfate, and the solution was filtered. The solvent was evaporated under reduced pressure, and the product was purified by column chromatography (using a mixture of methanol and dichloromethane, 1:20) to yield 5-(3,4-dimethoxyphenyl)-1,10-phenanthroline as a light-yellow solid.

Device fabrication

For the fabrication of small-area inverted perovskite solar cells, FTO substrates were first cleaned by sequential ultrasonic treatment in detergent, deionized water, ethanol, and a second rinse in deionized water, each for 15 min. Subsequently, a MeO-4PACz solution (0.7 mg/mL in IPA) was spin-coated onto the cleaned substrates at 5,000 rpm for 30 s and then annealed at 100°C for 15 min. In particular, the J5 molecule was added at a concentration of 1 mM. The perovskite film was formed from a precursor solution containing 1.5 M $Cs_{0.05}FA_{0.85}MA_{0.1}PbI_3$, dissolved in a mixed solvent of DMSO and DMF (1:4 by volume) and additionally comprising 10 mol % MACl and 5 mol % $PbCl_2$. This solution was spin-coated in two steps: first at 1,000 rpm for 10 s and then at 6,000 rpm for 35 s. During the final 7 s, 220 μL of chlorobenzene was dropped as an anti-solvent. The resulting wet film was then annealed at 100°C for 25 min. To passivate the perovskite surface, a PEAI solution (2 mg/mL) was spin-coated at 4,000 rpm for 30 s, followed by thermal treatment for 3 min. A PCBM electron transport layer (20 mg/mL in chlorobenzene) was then deposited at 2,000 rpm for 30 s, and a BCP interlayer (0.5 mg/mL) was spin-coated at 4,000 rpm for 30 s. Moreover, J2 was introduced at a concentration of 5 mM. Finally, a silver electrode (100 nm thick) was thermally evaporated to complete the device structure.

For the fabrication of inverted perovskite solar cells with an active area of 1 cm^2, the process followed was identical to that used for small-area devices, except that the amount of chlorobenzene employed as the anti-solvent was increased from 200 to 320 μL to accommodate the larger substrate size.

Characterization

The ^{1}H NMR spectra of J2 and J5 were recorded on a Bruker 400 MHz spectrometer using DMSO-d_6 as the solvent. X-ray photoelectron spectroscopy (XPS, Thermo Fisher Scientific ESCALAB 250Xi) was utilized to analyze the valence band variations of surface elements in the perovskite films. UPS was performed using an ESCALAB 250Xi system. The surface morphology was examined using scanning electron microscopy (SEM, Hitachi S-4800). Photoluminescence (PL) mapping was performed on a Nikon ARsiMP-LSM-Kit-Legend Elite-USX laser confocal fluorescence lifetime imaging microscope with a 405 nm excitation wavelength. Additionally, TRPL measurements were carried out using an FLS980 system to probe the carrier dynamics. To investigate the surface potential distribution, KPFM (FMNanoview 1000) was employed. The migration behavior of Pb^{2+} ions was characterized by time-of-flight secondary ion mass spectrometry (TOF-SIMS 5-100, IONTOF GmbH). For the *in situ* electroluminescence (EL) tests, a commercial dynamic spectrometer (Du-10, Puguangweishi Co.) was used. Atomic absorption spectrometry (AAS) was conducted on a Shimadzu AA7000 instrument, and GIXRD analysis was performed using a Micromax-007HF system.

The photovoltaic performance of the devices was characterized using a Keithley 2400 source meter, with a scan speed of 0.06 V/s under standard AM 1.5 G simulated sunlight and shadow masks defining active areas of 0.08 cm^2 and 1 cm^2. The EQE spectra and the corresponding integrated current were recorded with an Enli Tech QE-R measurement system. The operational stability of the devices was monitored under continuous illumination (AM 1.5 G) at a controlled temperature of 50 ± 5°C. For the temperature cycling reliability tests, a PL-80-2C temperature and humidity chamber (Lab Companion) was employed to perform thermal cycles between 25°C and 85°C at a relative humidity of 25%.

DFT calculations

DFT calculations were conducted using the Vienna *Ab initio* Simulation Package (VASP).[46,47] The exchange-correlation effects were treated with the Perdew-Burke-Ernzerhof (PBE) functional under the generalized gradient approximation (GGA) scheme.[48,49] The interactions between core and valence electrons were represented by the projector augmented-wave (PAW) method.[50] A plane-wave basis set with an energy cutoff of 400 eV was employed, and the Brillouin zone was sampled using a $2 \times 2 \times 1$ Monkhorst-Pack k-point mesh. Structural relaxations were performed until the total energy and atomic forces converged to thresholds of 1.0×10^{-4} eV and 0.05 eV $Å^{-1}$, respectively.

The adsorption energy (E_{ads}) is defined as:

$$E_{ads} = E_{complex} - E_{slab} - E_{cluster}$$

where slab and cluster refer to the metal surface and adsorbate molecule, respectively.

RESOURCE AVAILABILITY

Lead contact

Further information and requests for resources should be directed to and will be fulfilled by the lead contact, Meicheng Li (mcli@ncepu.edu.cn).

Materials availability

This study did not generate new unique materials.

Data and code availability

This study did not generate any datasets.

ACKNOWLEDGMENTS

This work is supported partially by the Beijing Natural Science Foundation (Z240024), National Natural Science Foundation of China (grant nos. 52232008, 52402254, 52102245, and 22409061), Beijing Nova Program (20220484016), Young Elite Scientists Sponsorship Program by CAST (2022QNRC001), Huaneng Group Headquarters Science and Technology Project (HNKJ20-H88), the Fundamental Research Funds for the Central Universities (2024MS036 and 2024JC005), and the NCEPU "Double First-Class" Program.

AUTHOR CONTRIBUTIONS

M.L., S.Q., and H.H. conceived the idea. M.L. and H.H. guided the work as supervisors. S.Q. and H.H. did experimental designs, device fabrication, and data analysis. F.Y., C.S., Q.Z., and T.J. were involved in device fabrication and conducted part of the characterizations. Y.Y. and L.Y. assisted with PL spectra testing. P.C. and Z.L. provided support for characterizing UPS testing. S.Q. and H.H. drafted the initial version of the manuscript. L.Y., Z.L., S.D., Z.W., and T.J. contributed to the manuscript revision and language polishing. All authors participated in discussing the results and contributed to revising the manuscript.

DECLARATION OF INTERESTS

The authors declare no competing interests.

SUPPLEMENTAL INFORMATION

Supplemental information can be found online at https://doi.org/10.1016/j.matt.2025.102525.

Received: August 17, 2025
Revised: October 8, 2025
Accepted: October 23, 2025

REFERENCES

1. He, D., Ma, D., Zhang, J., Yang, Y., Ding, J., Liu, C., Liu, X., Yu, Y., Liu, T., Chen, C., et al. (2025). Universal Ion Migration Suppression Strategy Based on Supramolecular Host–Guest Interaction for High-Performance Perovskite Solar Cells. Adv. Mater. *37*, 2505115. https://doi.org/10.1002/adma.202505115.
2. Wang, Y., Lin, R., Liu, C., Wang, X., Chosy, C., Haruta, Y., Bui, A.D., Li, M., Sun, H., Zheng, X., et al. (2024). Homogenized contact in all-perovskite tandems using tailored 2D perovskite. Nature *635*, 867–873.
3. Sun, X., Shi, W., Liu, T., Cheng, J., Wang, X., Xu, P., Zhang, W., Zhao, X., and Guo, W. (2025). Vapor-assisted surface reconstruction enables outdoor-stable perovskite solar modules. Science *388*, 957–963.
4. Chen, Y., Yang, N., Zheng, G., Pei, F., Zhou, W., Zhang, Y., Li, L., Huang, Z., Liu, G., Yin, R., et al. (2024). Nuclei engineering for even halide distribution in stable perovskite/silicon tandem solar cells. Science *385*, 554–560.
5. Jia, Z., Guo, X., Yin, X., Sun, M., Qiao, J., Jiang, X., Wang, X., Wang, Y., Dong, Z., Shi, Z., et al. (2025). Efficient near-infrared harvesting in perovskite–organic tandem solar cells. Nature *643*, 104–110.
6. Liu, S., Li, J., Xiao, W., Chen, R., Sun, Z., Zhang, Y., Lei, X., Hu, S., Kober-Czerny, M., Wang, J., et al. (2024). Buried interface molecular hybrid for inverted perovskite solar cells. Nature *632*, 536–542.

7. Yu, S., Xiong, Z., Zhou, H., Zhang, Q., Wang, Z., Ma, F., Qu, Z., Zhao, Y., Chu, X., Zhang, X., and You, J. (2023). Homogenized NiO_x nanoparticles for improved hole transport in inverted perovskite solar cells. Science *382*, 1399–1404.

8. Yang, Y., Chen, H., Liu, C., Xu, J., Huang, C., Malliakas, C.D., Wan, H., Bati, A.S.R., Wang, Z., Reynolds, R.P., et al. (2024). Amidination of ligands for chemical and field-effect passivation stabilizes perovskite solar cells. Science *386*, 898–902.

9. Luo, C., Zhou, Q., Wang, K., Wang, X., He, J., Gao, P., Zhan, C., Bi, Z., Li, W., Ma, Y., et al. (2025). Engineering bonding sites enables uniform and robust self-assembled monolayer for stable perovskite solar cells. Nat. Mater. *24*, 1265–1272. https://doi.org/10.1038/s41563-025-02275-x.

10. Liu, C., Yang, Y., Fletcher, J.D., Liu, A., Gilley, I.W., Musgrave III, C.B., Wang, Z., Zhu, H., Chen, H., Reynolds, R.P., et al. (2025). Cation interdiffusion control for 2D/3D heterostructure formation and stabilization in inorganic perovskite solar modules. Nat. Energy *10*, 981–990. https://doi.org/10.1038/s41560-025-01817-6.

11. Li, Z., Guo, P., Zhang, Y., Wang, W., Cai, S., and Zhou, Y. (2025). Synthesis of a lattice-resolved laminate-structured perovskite heterointerface. Nat. Synth. *4*, 1078–1087. https://doi.org/10.1038/s44160-025-00787-7.

12. Chen, J., Wang, X., Wang, T., Li, J., Chia, H.Y., Liang, H., Xi, S., Liu, S., Guo, X., Guo, R., et al. (2025). Determining the bonding–degradation trade-off at heterointerfaces for increased efficiency and stability of perovskite solar cells. Nat. Energy *10*, 181–190.

13. Tang, X., Yang, C., Xu, Y., Xia, J., Li, B., Li, M., Zhou, Y., Jiang, L., Liu, H., Ma, K., et al. (2025). Enhancing the efficiency and stability of perovskite solar cells via a polymer heterointerface bridge. Nat. Photon. *19*, 701–708. https://doi.org/10.1038/s41566-025-01676-3.

14. Zhan, L., Zhang, S., Gao, W., Zheng, W., Li, Z., Jiang, X., Ning, Z., Han, L., Li, Z., Stolterfoht, M., et al. (2025). Reinforced Perovskite-Substrate Interfaces via Multi-Sited and Dual-Sided Anchoring. Adv. Mater. *37*, 2506048. https://doi.org/10.1002/adma.202506048.

15. Duan, T., You, S., Chen, M., Yu, W., Li, Y., Guo, P., Berry, J.J., Luther, J.M., Zhu, K., and Zhou, Y. (2024). Chiral-structured heterointerfaces enable durable perovskite solar cells. Science *384*, 878–884.

16. Cai, Z., Yao, Z., Xing, Z., Dai, R., Huang, Z., Meng, X., Hu, X., and Chen, Y. (2025). A Buried Interface Fastening Approach for Efficient and Flexible Perovskite Photovoltaics. Adv. Funct. Mater. *35*, 2505921. https://doi.org/10.1002/adfm.202505921.

17. Li, X., Xu, Z., Zhao, R., Ge, S., Liu, T., Cai, B., Li, M., and Zhang, W.H. (2025). Multifunctional Interfacial Molecular Bridging Strategy Enables Efficient and Stable Inverted Perovskite Solar Cells. Adv. Mater. *37*, 2508352. https://doi.org/10.1002/adma.202508352.

18. Zhao, W., Guo, P., Su, J., Fang, Z., Jia, N., Liu, C., Ye, L., Ye, Q., Chang, J., and Wang, H. (2022). Synchronous passivation of defects with low formation energies via terdentate anchoring enabling high performance perovskite solar cells with efficiency over 24%. Adv. Funct. Mater. *32*, 2200534.

19. Gong, C., Li, H., Wang, H., Zhang, C., Zhuang, Q., Wang, A., Xu, Z., Cai, W., Li, R., Li, X., and Zang, Z. (2024). Silver coordination-induced n-doping of PCBM for stable and efficient inverted perovskite solar cells. Nat. Commun. *15*, 4922.

20. Fei, C., Li, N., Wang, M., Wang, X., Gu, H., Chen, B., Zhang, Z., Ni, Z., Jiao, H., Xu, W., et al. (2023). Lead-chelating hole-transport layers for efficient and stable perovskite minimodules. Science *380*, 823–829.

21. Huang, X., Xia, D., Xie, Q., Wang, D., Li, Q., Zhao, C., Yin, J., Cao, F., Su, Z., Zeng, Z., et al. (2025). Supramolecular force-driven non-fullerene acceptors as an electron-transporting layer for efficient inverted perovskite solar cells. Nat. Commun. *16*, 1626.

22. Fei, C., Kuvayskaya, A., Shi, X., Wang, M., Shi, Z., Jiao, H., Silverman, T.J., Owen-Bellini, M., Dong, Y., Xian, Y., et al. (2024). Strong-bonding hole-transport layers reduce ultraviolet degradation of perovskite solar cells. Science *384*, 1126–1134.

23. Wang, X., Li, J., Guo, R., Yin, X., Luo, R., Guo, D., Ji, K., Dai, L., Liang, H., Jia, X., et al. (2024). Regulating phase homogeneity by self-assembled molecules for enhanced efficiency and stability of inverted perovskite solar cells. Nat. Photon. *18*, 1269–1275. https://doi.org/10.1038/s41566-024-01531-x.

24. Li, M., Liu, M., Qi, F., Lin, F.R., and Jen, A.K.Y. (2024). Self-assembled monolayers for interfacial engineering in solution-processed thin-film electronic devices: design, fabrication, and applications. Chem. Rev. *124*, 2138–2204.

25. Zhang, X., Li, B., Zhang, S., Lin, Z., Han, M., Liu, X., Chen, J., Du, W., Rahim, G., Zhou, Y., et al. (2025). A spiro-type self-assembled hole transporting monolayer for highly efficient and stable inverted perovskite solar cells and modules. Energy Environ. Sci. *18*, 468–477.

26. Du, J., Chen, J., Ouyang, B., Sun, A., Tian, C., Zhuang, R., Chen, C., Liu, S., Chen, Q., Li, Z., et al. (2025). Face-on oriented self-assembled molecules with enhanced π–π stacking for highly efficient inverted perovskite solar cells on rough FTO substrates. Energy Environ. Sci. *18*, 3196–3210.

27. Li, D., Lian, Q., Du, T., Ma, R., Liu, H., Liang, Q., Han, Y., Mi, G., Peng, O., Zhang, G., et al. (2024). Co-adsorbed self-assembled monolayer enables high-performance perovskite and organic solar cells. Nat. Commun. *15*, 7605.

28. Wang, J., Zheng, L., Kim, H.B., He, H., Wang, S., Eickemeyer, F.T., Jo, Y., Zhao, Y., Wei, M., Jeong, J., et al. (2025). Dipolar Carbazole Ammonium for Broadened Electric Field Distribution in High-Performance Perovskite Solar Cells. J. Am. Chem. Soc. *147*, 8663–8671.

29. Huang, H., Cui, P., Chen, Y., Yan, L., Yue, X., Qu, S., Wang, X., Du, S., Liu, B., Zhang, Q., et al. (2022). 24.8%-efficient planar perovskite solar cells via ligand-engineered TiO_2 deposition. Joule *6*, 2186–2202.

30. Yan, L., Huang, H., Cui, P., Du, S., Lan, Z., Yang, Y., Qu, S., Wang, X., Zhang, Q., Liu, B., et al. (2023). Fabrication of perovskite solar cells in ambient air by blocking perovskite hydration with guanabenz acetate salt. Nat. Energy *8*, 1158–1167.

31. Li, F., Deng, X., Qi, F., Li, Z., Liu, D., Shen, D., Qin, M., Wu, S., Lin, F., Jang, S.H., et al. (2020). Regulating surface termination for efficient inverted perovskite solar cells with greater than 23% efficiency. J. Am. Chem. Soc. *142*, 20134–20142.

32. Liu, Z., Lin, R., Wei, M., Yin, M., Wu, P., Li, M., Li, L., Wang, Y., Chen, G., Carnevali, V., et al. (2025). All-perovskite tandem solar cells achieving> 29% efficiency with improved (100) orientation in wide-bandgap perovskites. Nat. Mater. *24*, 252–259.

33. Cheng, J., Cao, H., Zhang, S., Shao, J., Yan, W., Peng, C., Yue, F., and Zhou, Z. (2024). Enhanced Electric Field Minimizing Quasi-Fermi Level Splitting Deficit for High-Performance Tin-Lead Perovskite Solar Cells. Adv. Mater. *36*, 2410298.

34. Chen, H., Liu, C., Xu, J., Maxwell, A., Zhou, W., Yang, Y., Zhou, Q., Bati, A.S.R., Wan, H., Wang, Z., et al. (2024). Improved charge extraction in inverted perovskite solar cells with dual-site-binding ligands. Science *384*, 189–193.

35. Zhang, P., Zhu, C., Su, W., Wang, S., Xu, Z., Wang, S., Qi, M., Bao, X., Kang, F., Hao, T., et al. (2025). Carrier Dynamics of Facet-Dependent Heterogeneous Interfaces in High-Performance Perovskite Solar Cells. Adv. Funct. Mater. *35*, 2422783.

36. Liu, H., Lu, Z., Zhang, W., Wang, J., Lu, Z., Dai, Q., Qi, X., Shi, Y., Hua, Y., Chen, R., et al. (2022). Anchoring Vertical Dipole to Enable Efficient Charge Extraction for High-Performance Perovskite Solar Cells. Adv. Sci. *9*, 2203640.

37. Qu, S., Yang, F., Huang, H., Li, Y., Sun, C., Zhang, Q., Du, S., Yan, L., Lan, Z., Wang, Z., et al. (2025). Redox mediator-modified self-assembled monolayer stabilizes a buried interface in efficient inverted perovskite solar cells. Energy Environ. Sci. *18*, 3186–3195.

38. Tao, M., Wang, Y., Zhang, K., Song, Z., Lan, Y., Guo, H., Guo, L., Zhang, X., Wei, J., Cao, D., and Song, Y. (2024). Molecule-triggered strain

regulation and interfacial passivation for efficient inverted perovskite solar cells. Joule *8*, 3142–3152.

39. Zhang, H., and Park, N.G. (2022). Strain control to stabilize perovskite solar cells. Angew. Chem. Int. Ed. *61*, e202212268.
40. Cheng, M., Duan, Y., Zhang, D., Xie, Z., Li, H., Cao, Q., Qiu, Z., Chen, Y., and Peng, Q. (2025). Tailoring Buried Interface and Minimizing Energy Loss Enable Efficient Narrow and Wide Bandgap Inverted Perovskite Solar Cells by Aluminum Glycinate Based Organometallic Molecule. Adv. Mater. *37*, 2419413.
41. Du, S., Huang, H., Lan, Z., Cui, P., Li, L., Wang, M., Qu, S., Yan, L., Sun, C., Yang, Y., et al. (2024). Inhibiting perovskite decomposition by a creeper-inspired strategy enables efficient and stable perovskite solar cells. Nat. Commun. *15*, 5223.
42. Zhuang, X., Zhou, D., Jia, Y., Liu, S., Liang, J., Lin, Y., Hou, H., Qian, D., Zhou, T., Bai, X., and Song, H. (2024). Bottom-Up Defect Modification Through Oily-Allicin Modified Buried Interface Achieving Highly Efficient and Stable Perovskite Solar Cells. Adv. Mater. *36*, 2403257.
43. Shao, Y., Xiao, Z., Bi, C., Yuan, Y., and Huang, J. (2014). Origin and elimination of photocurrent hysteresis by fullerene passivation in $CH_3NH_3PbI_3$ planar heterojunction solar cells. Nat. Commun. *5*, 5784.
44. Ma, Y., Zeng, C., Zeng, P., Hu, Y., Li, F., Zheng, Z., Qin, M., Lu, X., and Liu, M. (2023). How do surface polar molecules contribute to high open-circuit voltage in perovskite solar cells? Adv. Sci. *10*, 2205072.
45. Liu, H., Zhang, Z., Shi, Y., Ran, W., Zhong, H., and Zhang, F. (2025). A low-cost and bendable "cage" for stable rigid and flexible perovskite solar cells with negligible lead leakage. Joule *9*, 101816.
46. Kresse, G., and Hafner, J. (1993). *Ab initio* molecular dynamics for liquid metals. Phys. Rev. B *47*, 558–561.
47. Kresse, G., and Hafner, J. (1994). *Ab initio* molecular-dynamics simulation of the liquid-metal–amorphous-semiconductor transition in germanium. Phys. Rev. B *49*, 14251–14269.
48. Perdew, J.P., Burke, K., and Ernzerhof, M. (1996). Generalized gradient approximation made simple. Phys. Rev. Lett. *77*, 3865–3868.
49. Kresse, G., and Joubert, D. (1999). From ultrasoft pseudopotentials to the projector augmented-wave method. Phys. Rev. B *59*, 1758–1775.
50. Blöchl, P.E. (1994). Projector augmented-wave method. Phys. Rev. B *50*, 17953–17979.